

Controlled-SWAP gates by tuning of interfering transition pathways in neutral atom arrays

Mohommadsadegh Khazali¹, Klaus Mølmer²

¹ Dept of Physics, University of Tehran, Tehran, Iran

² Niels Bohr Institute, Jagtvej 155 A, 2200 Copenhagen, Denmark

Neutral-atom quantum processors employ Rydberg blockade for multiqubit phase operations but lack similar native exchange and conditional exchange gates, which are essential primitives for state verification, fermionic and XY-model simulation, and efficient routing in large qubit arrays. We show that by lifting the degeneracy between interfering transition pathways, a single Rydberg excited atom can control state exchange between pairs of atoms. Using this mechanism, we realize a direct controlled-SWAP (Fredkin) operation with more than 99% fidelity and an order-of-magnitude reduction in circuit depth and reduced exposure to decay and decoherence of Rydberg state components compared with decomposed implementations. The mechanism operates robustly under Doppler broadening at 150 μK and realistic laser-intensity noise and extends naturally to an entire family of useful gates, including multi-control conditional exchanges (C_k -SWAP) and conditional multiplexed SWAP gates. By incorporating controlled exchange operations as native physical operations on neutral atoms, our work provides multiqubit gates that enable higher-order state-verification protocols, occupation-dependent simulations, and conditional routing across optical lattices.

I. INTRODUCTION

Highly excited Rydberg atoms have emerged as a powerful platform for quantum technologies [1–25]. Rydberg-based quantum processors have established two- and multi-qubit phase gates as their native building blocks [26–44]. These controlled-phase operations have enabled scalable entanglement and collective logic, yet they must be combined with single-qubit operations to yield the exchange processes that are indispensable for state verification and purity measurement, e.g., through the SWAP test [45–49], for fermionic and XY-model simulation [50–53], and for efficient routing in two-dimensional processor layouts [54]. In particular, the controlled-SWAP (Fredkin) gate provides a direct means to estimate overlaps and nonlinear functionals of quantum states without state tomography [46–48], serves as a core element for entanglement fusion and routing in multipartite networks [55], and even appears in joint-measurement and weak-value extraction protocols [56]. Modern variants extend this idea to variational overlap learning and quantum kernel estimation [49], underscoring that controlled exchange constitutes a key verification primitive even in today’s NISQ processors. Moreover, exchange-type couplings naturally implement the quantum-walk Hamiltonian, which is universal for quantum computation and underlies topological and fermionic simulation [58, 59]. These diverse applications highlight the Fredkin gate’s central role across quantum information, simulation, and measurement science.

In quantum simulation, exchange couplings underpin the XY Hamiltonian, which is directly generated by iSWAP and $\sqrt{\text{SWAP}}$ gates [50] and forms the basis of spin-exchange and fermionic models [53]. Native exchange interactions have enabled fermionic hopping and localization studies on superconducting platforms [51], and multipartite entanglement and XY dynamics in

large-scale processors [52]. Yet, on neutral atoms, such exchange gates are only emulated through long decompositions of native phase operations [57], inflating circuit depth, calibration complexity, and the susceptibility to spontaneous emission and black-body radiation. This, in turn, degrades simulation fidelity, and makes SWAP-based routing prohibitively expensive [54].

Routing and connectivity limitations in neutral-atom arrays have been mitigated experimentally through physical atom transport and rearrangement [60], yet such mechanical solutions do not eliminate logical routing overhead. A truly scalable processor requires native logical exchange that operates across fixed lattice sites, and routing with nearest-neighbour SWAP gates would still require a large overhead [54]. With our protocol, using long-range interaction, direct exchange between far-separated qubits accelerates the routing process.

Here, we introduce interaction-enabled destructive interference as a general synthesis principle for non-diagonal multiqubit gates. In our scheme, a collective Rydberg excitation mediates a resonant four-photon exchange between target qubit states $|01\rangle$ and $|10\rangle$. All other computational states remain far detuned or evolve into dark states, ensuring perfect state retrieval and completing the SWAP operation. Extending this mechanism to a controlled-SWAP (Fredkin) gate, the interaction between a control qubit and a target pair determines which interference channel is active. Depending on the control state, the target pair adiabatically follows distinct interaction-dependent eigenmodes, so that the SWAP is conditionally enabled or suppressed. Implemented on neutral atoms, this approach realizes a single-step controlled-SWAP and its exchange family with phase programmability. Here, we avoid fragile anti-blockade conditions as in previous proposals [61], which encounter significant practical limitations due to their sensitivity to Doppler-induced detunings and fluctuations in interatomic spacing.

We show that the interference-based scheme can naturally extend to multi-control SWAPs and conditional multiplexed SWAPs, enabling conditional exchange among several registers. Such gates can support multi-copy state-verification protocols, occupation-dependent tunneling in correlated-fermion simulations, and data-selective routing or code-block exchange in scalable quantum architectures. Quantitatively, the direct controlled-SWAP and its exchange variants reduce circuit depth and Rydberg exposure by more than an order of magnitude compared to standard decompositions, and our numerical simulations show fidelities above 99%, even when the atoms are subject to realistic laser-intensity noise and Doppler broadening at 150 μK temperature.

Treating exchange as a native primitive broadens the algorithmic reach of neutral-atom processors and, more broadly, our work establishes interaction-enabled interference as a general synthesis principle, turning mediated exchange channels on or off through a controllable near-degeneracy. Similar interference mechanisms may apply in other platforms and architectures where it may unify verification, simulation, and scalable compilation across diverse quantum technologies.

The article is organized as follows. In Sec. II, we introduce the controlled-SWAP (Fredkin) scheme based on interaction-enabled interference and discuss the effective Hamiltonian governing its dynamics. Section III quantifies the gate performance under realistic experimental imperfections and highlights its robustness and operational advantages. In Sec. IV, we generalize the mechanism to multi-control and conditional multiplexed SWAP configurations, demonstrating programmable multi-qubit exchange across extended lattice geometries. Finally, Sec. V discusses the broader implications of this approach in neutral-atom processors.

II. CONTROLLED-SWAP SCHEME

The level scheme of C-SWAP, shown in Fig. 1, consists of logical states $|0\rangle$ and $|1\rangle$ corresponding to hyperfine ground states, while $|r\rangle$ denotes a high lying Rydberg level. The logical rotations between $|0\rangle$ and $|1\rangle$ are driven by a microwave field with Rabi frequency Ω_1 [62], whereas the Rydberg excitation processes are implemented optically with Rabi frequencies Ω_c and Ω_2 . The gate operates through the following three steps:

- (i) *Control excitation:* A π pulse transfers the control atom from $|0\rangle$ into the Rydberg state $|r\rangle$.
- (ii) *Target driving:* Simultaneously, the two target atoms are driven by fields Ω_1 and Ω_2 , coupling $|0\rangle \rightarrow |r\rangle$ via (but detuned from) the other qubit state $|1\rangle$. When the control atom occupies $|r\rangle$, the Rydberg-Rydberg interaction shifts the target levels, engineering destructive interference that blocks the SWAP. Conversely, if the control remains in $|1\rangle$, the target system undergoes the SWAP operation.
- (iii) *Control retrieval:* A second π pulse returns the

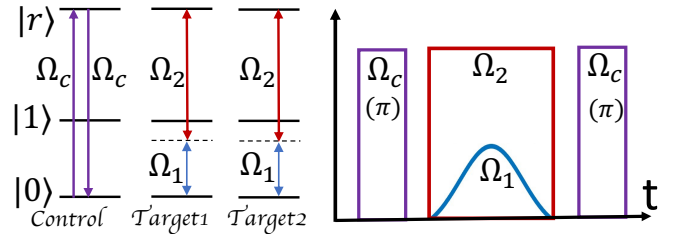


FIG. 1. Level Scheme and the time diagram of the laser pulse orders for the controlled-SWAP operation

control atom from $|r\rangle$ back to $|0\rangle$, completing the gate.

To explain the physics behind the controlled-SWAP operation, we consider the Hamiltonian governing step (ii), in the collective basis of the two target atoms for the case initialized in the state $|01\rangle$, see Fig. 2(a1,a2)

$$\begin{aligned} H_t = & \frac{\Omega_1}{2} [(|01\rangle + |10\rangle)(\langle 11| + \langle 00|) + \text{h.c.}] \quad (1) \\ & + \frac{\sqrt{2}\Omega_2}{2} (|\overline{1r}\rangle\langle 11| + \text{h.c.}) + \frac{\Omega_2}{2} (|r0\rangle\langle 10| + |01\rangle\langle 0r| + \text{h.c.}) \\ & + \Delta (|11\rangle\langle 11| - |00\rangle\langle 00|) + \delta_r |\overline{r1}\rangle\langle \overline{r1}| \\ & + (-\Delta + \delta_r) (|0r\rangle\langle 0r| + |r0\rangle\langle r0|) \end{aligned}$$

where $|\overline{1r}\rangle = (|1r\rangle + |r1\rangle)/\sqrt{2}$, and the detuning induced by the control-target interaction $\delta_r = V$ if the control atom is in $|r_c\rangle$, and $\delta_r = 0$ if in $|1_c\rangle$. The doubly excited state $|rr\rangle$ is neglected since it is energetically inaccessible due to the Rydberg blockade.

Examining the pathways of SWAP operation $|01\rangle\langle 10|$ in Fig. 2(a2), we observe that the second-order transitions via $|00\rangle$ and $|11\rangle$, with amplitudes $-\Omega_1^2/4\Delta$ and $\Omega_1^2/4\Delta$ respectively, exactly cancel each other out. This cancellation aligns with expectations since these paths do not involve any interacting states. The SWAP operation is enabled by the Rydberg blockade through a coherent four-photon transition sequence

$$|10\rangle \xrightarrow{\Omega_1} |11\rangle \xrightarrow{\sqrt{2}\Omega_2} |\overline{1r}\rangle \xrightarrow{\sqrt{2}\Omega_2} |11\rangle \xrightarrow{\Omega_1} |01\rangle. \quad (2)$$

Assuming a large detuning $\Delta \gg \Omega_1, \Omega_2$, we can adiabatically eliminate the off-resonant states in Fig. 2(a1,a2) reducing the dynamics to the subspace $\{|01\rangle, |10\rangle, |\overline{1r}\rangle\}$, with an effective Hamiltonian of

$$\begin{aligned} H = & A [(|01\rangle + |10\rangle)\langle \overline{1r}| + \text{h.c.}] \quad (3) \\ & + B |\overline{r1}\rangle\langle \overline{1r}| + C (|01\rangle\langle 01| + |10\rangle\langle 10|) \end{aligned}$$

where the introduced parameters are

$$A = \frac{\sqrt{2}\Omega_1\Omega_2}{4\Delta}; \quad B = V - \frac{2\Omega_2^2}{4\Delta}; \quad C = \frac{\Omega_2^2}{4(\Delta-V)}. \quad (4)$$

The residual coupling between $|10\rangle$ and $|01\rangle$ appears at the fourth-order perturbation, yielding the effective Rabi frequency $\Omega_{\text{eff}} = A^2/(B - C)$. In case of $|1_c\rangle$, in the absence of control-target interaction $V=0$, the effective

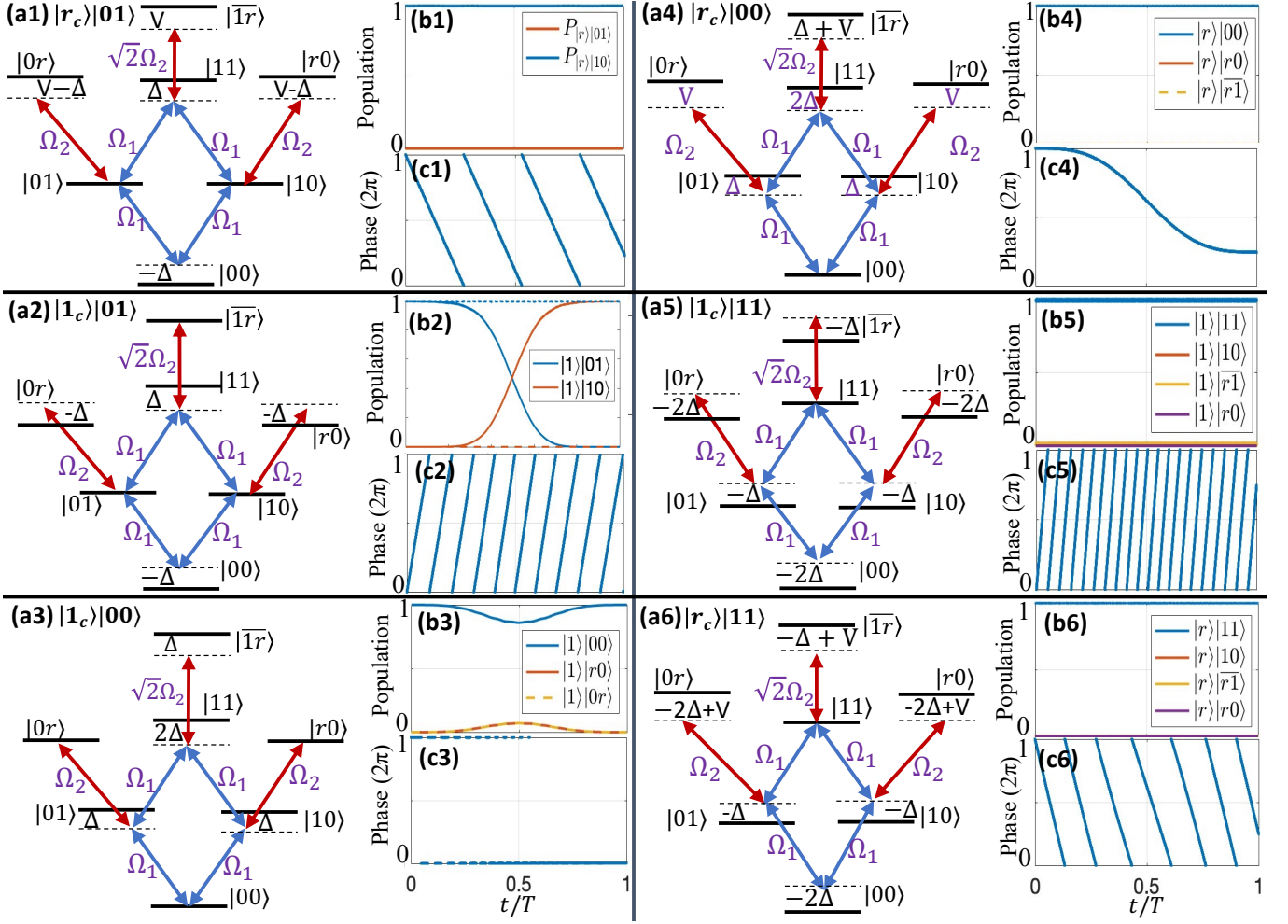


FIG. 2. **Controlled-SWAP Operation** – Panels 1–6 illustrate the operation for different qubit configurations. Series (a) shows the level scheme in the collective basis of the target atoms. Series (b) and (c) depict, respectively, the population dynamics and phase evolution during the application of the target pulses in step (ii) of gate operation. (a1,b1) When the control atom is in the Rydberg state $|r\rangle$ and targets are in $|10\rangle$ or $|01\rangle$, the interaction with the target atoms shifts the energy levels such that two eigenstates of Eq. 1 become nearly degenerate. This degeneracy leads to *destructive interference*, effectively blocking the SWAP between target atoms. (a2,b2) In the absence of control Rydberg excitation, the four-photon transition via the symmetric state $|1\bar{r}\rangle$ enables the SWAP between $|01\rangle$ and $|10\rangle$. Note that it is essential that neither of the target atoms is Rydberg-blocked by the control atom. The dashed lines in (b2) correspond to a case where one of the targets is blocked by the control under a non-isotropic interaction, illustrating that the SWAP operation cannot proceed via $|1r\rangle$ or $|r1\rangle$ alone but requires the symmetric state $|1\bar{r}\rangle = (|1r\rangle + |r1\rangle)/\sqrt{2}$. The same principle will be employed for a conditional multiplexed SWAP operation in the end of the paper. (a3) For the initial state $|1_c\rangle|00\rangle_t$, the only resonant two-photon transitions are to $|0r\rangle$ and $|r0\rangle$, which form a dark state with zero eigen energy, see text and hence generate no phase, see (c3), but it acquires a transient excited state population proportional to $(\Omega_1(t)/\Omega_2)^2$ until the system returns fully to $|00\rangle$ at the end of the Gaussian pulse, see (b3). All other computational basis states, including $|100\rangle$, $|r11\rangle$, and $|111\rangle$, involve far-detuned transitions and thus preserve their populations throughout the operation, see panels (b4, b5, b6), while acquiring phases due to AC Stark shift as quantified in panels (c4, c5, c6) and in the text. Applied parameters are presented in Table I. The gate output amplitudes are tabulated in Table III consistent with the desired controlled SWAP gates.

Rabi frequency would be $\Omega_{\text{eff}} = \frac{\Omega_1^2}{6\Delta}$. Hence, the SWAP time is given by

$$\int_{t=0}^T \frac{\Omega_1(t)^2}{6\Delta} dt = \pi. \quad (5)$$

In contrast, when the control is excited from $|0_c\rangle$ to the Rydberg level $|r_c\rangle$, in the desired operation regime

$|V|, |\Delta| \gg \Omega_2 > \Omega_1$ and $|V - \Delta| \gtrsim \Omega_2$, explained in Fig. 4, the swapping rate would be negligible, $\frac{\Omega_{\text{eff},r_c}}{\Omega_{\text{eff},1_c}} \approx \frac{\Omega_2^2}{V\Delta} \ll 1$. One should note that in the four-photon process described in Eq. 2, the SWAP operation proceeds only via the symmetric collective state $(|1r\rangle + |r1\rangle)/\sqrt{2}$. If either target qubit is blocked by the Rydberg control state, the transition pathway through an individual exci-

tation, such as $|1r\rangle$ or $|r1\rangle$, becomes inaccessible, and the SWAP process is consequently blocked, see dashed lines in Fig. 2(b2).

The physics behind the conditional blocking of the swap operation lies in the destructive quantum interference of overlapping eigenstates. The eigenstates of Eq. 3 are

$$|\beta_0\rangle = \frac{1}{\sqrt{2}}(|01\rangle - |10\rangle),$$

$$|\beta_{\mp}\rangle = \mathcal{N}_{\mp}[2A(|01\rangle + |10\rangle) + (\lambda_{\mp} - C)|\overline{r1}\rangle]. \quad (6)$$

with eigenvalues $\lambda_0 = C$, $\lambda_{\pm} = \frac{B+C \pm \sqrt{8A^2 + (B-C)^2}}{2}$, and \mathcal{N}_{\pm} being the normalization factor. Having the control in the Rydberg state $|r_c\rangle$, in the operation regime of parameters explained above, the two lower energy eigenstates become degenerate $\lambda_- \approx \lambda_0 = C < 0$. The system follows the collective degenerate state $(|\beta_0\rangle + |\beta_-\rangle)/\sqrt{2} \approx |01\rangle$, which remains in the initial state $|01\rangle$ due to destructive interference between the two eigen states, blocking the SWAP, as shown in Fig. 2(a1,b1).

In addition to the qubit rotation, the accumulated phase is tracked in Figs. 2(c1) and 2(c2). In case of $|r_c\rangle|01\rangle$, the phase is generated by the second-order lightshifts with couplings of $|01\rangle$ to $|00\rangle$, $|11\rangle$, $|0r\rangle$, see Fig. 2(a1). The first two cancel each other due to opposite detunings, leaving the third term $\Delta E_{|r_c01\rangle}^{(2)} = \Omega_2^2/4(\Delta - V)$. The acquired phase would be $\phi_{|r_c01\rangle} = \Omega_2^2 T/4(\Delta - V)$, where T is the operation time, defined in Eq. 5. In case of $|1_c\rangle|01\rangle$ with the level scheme of Fig. 2(a2), the similar result with $V = 0$ leads to the phase of $\phi_{|1_c01\rangle} = \Omega_2^2 T/4\Delta$.

Considering the initial qubit configuration $|1\rangle_c|00\rangle_t$, the collective level scheme depicted in Fig. 2(a3), supports resonant two-photon transitions to the singly excited Rydberg states $|0r\rangle$ and $|r0\rangle$. The off-resonant transitions to $|11\rangle$ and $|\overline{1r}\rangle$ only generate an AC-Stark shift that modifies the detunings of $|01\rangle$ and $|10\rangle$ states to Δ' , and effectively, both states could be adiabatically eliminated, simplifying the Hamiltonian to

$$H = \frac{\Omega_1}{2}(|01\rangle + |10\rangle)\langle 00| + \frac{\Omega_2}{2}(|0r\rangle\langle 01| + |r0\rangle\langle 10|) + \text{h.c.}$$

$$+ \Delta'(|01\rangle\langle 01| + |10\rangle\langle 10|), \quad (7)$$

which has a dark eigenstate of the form

$$|D(t)\rangle = \frac{\Omega_2|00\rangle - \Omega_1(t)(|0r\rangle + |r0\rangle)}{\sqrt{2\Omega_1(t)^2 + \Omega_2^2}}. \quad (8)$$

Under adiabatic evolution with a Gaussian-shaped $\Omega_1(t)$ pulse and assuming $\Omega_1 \ll \Omega_2$, the system temporarily populates $|0r\rangle$ and $|r0\rangle$ with probability $P(t) = \Omega_1(t)^2/\Omega_2^2$, yet ultimately returns to the initial state $|00\rangle$, see Fig. 2(b3). Since the system follows the dark eigenstate with a constant zero eigenvalue, it acquires no phase, as shown in Fig. 2(c3).

In contrast, applying the target pulses to the initial state $|r\rangle_c|00\rangle_t$, with the level structure of Fig. 2(a4),

the control-target Rydberg interaction far-detunes all transitions, thus breaking the resonance and suppressing any population transfer, as illustrated in Fig. 2(b4). Nonetheless, a dynamical phase is accumulated as depicted in Fig. 2(c4). Considering the operation regime of $\Omega_1 < \Omega_2 \ll (\Delta, \Delta + V, \Delta - V, V)$ the dominant lightshift comes from the second order couplings of $|00\rangle$ with $|01\rangle$ and $|10\rangle$ adding up to $2 \times \frac{\Omega_1(t)^2}{4\Delta}$. The fourth-order light shift going from $|00\rangle$ to $|0r\rangle$ or $|r0\rangle$ and back generates $\Delta E^{(4)} = -\frac{\Omega_1^2 \Omega_2^2}{8\Delta^2 V}$, which is negligible considering the regime of operation mentioned above. The coupling to $|\overline{1r}\rangle$ would be an even smaller sixth-order lightshift, and is also negligible. Hence, the acquired phase over the gate operation time T defined by Eq. 5 would be $\phi_{|0_c\rangle|00\rangle} = -3\pi/2$. This would be independent of the laser control parameters, and any deviation from this value would be attributed to the small fourth-order effect.

In qubit configurations $|r_c\rangle|11\rangle$ and $|1_c\rangle|11\rangle$, all the transitions are far detuned and hence the population transfer is minor. In case of $|r_c\rangle|11\rangle$ the dominant lightshift $\Delta E_{r_c11} = 2\frac{\Omega_1^2}{4\Delta} + \frac{\Omega_2^2}{2(\Delta - V)}$ comes from the second order detuned coupling of $|11\rangle$ with $|\overline{1r}\rangle$, $|10\rangle$ and $|01\rangle$, see Fig. 2(a6). The accumulated phase after the operation time T would be $\phi_{r_c11} = 3\pi + \frac{\Omega_2^2 T}{2(\Delta - V)}$. In case of $|1_c\rangle|11\rangle$ with the level scheme of Fig. 2(a5), a similar level scheme with the absence of control-target interaction $V = 0$ leads to the phase of $\phi_{1_c11} = 3\pi + \frac{\Omega_2^2 T}{2\Delta}$.

Finally, the presented scheme can realize multiple SWAP-type gates, by omitting the control atom and tuning the pulse parameters listed in Table I. Final phase adjustment can be applied with $R(\phi) = |0\rangle\langle 0| + \exp(i\phi)|1\rangle\langle 1|$, and the so-called bSWAP operation can be realized as bSWAP = $(\text{IX})(\text{SWAP})(\text{IX})$. The resulting error budgets for population rotation, phase adjustment, and Rydberg-state decay of all variants are compiled for each qubit configuration in Tables II and III.

III. PERFORMANCE, ROBUSTNESS AND OPERATIONAL ADVANTAGES

Here, we quantify the gate operation and discuss its advantages compared to previous anti-blockade schemes, emphasizing its robustness against realistic experimental imperfections. We also highlight the potential to operate between non-adjacent sites across the lattice. To quantify the gate fidelity, we use a definition that encounters population rotation and phase accuracy [65],

$$F = [\text{Tr}(MM^\dagger) + |\text{Tr}(M)|^2]/[n(n+1)] \quad (9)$$

with $M = U_{id}^\dagger U_{gate}$, where U_{id} and U_{gate} , represents ideal and realistic gate operations. U_{gate} is obtained from numerical simulation of the gate for all the possible 8-qubit product state configurations.

Gate type	$\Omega_2/2\pi$ (MHz)	$\Delta/2\pi$ (MHz)	Fid (%)	Ryd loss	Final Phase adj. [atom #]
iSWAP	145.82	999.84	99.2	0.00017	$-\pi/2$ [1,2]
SWAP	190.8	999.73	99.66	0.00017	-0.2971π [1,2]
\sqrt{iSWAP}	137.56	1000.3	99.15	0.0001	—
C-iSWAP	145.82	1000.3	98.9	0.0052	$-\pi/2$ [c, t_1, t_2]
CCS [†] .CSWAP	89.76	1001.2	99.34	0.0052	$\pi/2$ [c]

TABLE I. Realization of various SWAP and controlled-SWAP (C-SWAP) gate variants by tuning the control parameters. Gate accuracy is quantified by the process fidelity, which captures both rotation-angle precision and phase-accumulation errors. The loss from the Rydberg state, averaged over all qubit configurations, is presented separately. Applying a final single-qubit phase shift to the excited states of the indicated qubits yields the desired operation. Although high fidelity benefits from precise parameter tuning, the scheme tolerates realistic fluctuations in the experiment (see Fig. 3,4). Applied parameters are $\Omega_1(t)/2\pi = 33.5 \left(e^{-\frac{(t-T/2)^2}{2\sigma^2}} - e^{-\frac{(T/2)^2}{2\sigma^2}} \right)$ MHz, interaction between target atoms $V_{tt}/2\pi = 700$ MHz, control-target interaction $V_{c-t} = 24.8$ and 22.14GHz for C-iSWAP and C-SWAP respectively. Gaussian pulse width $\sigma = T/4$, and pulse duration is $T = 4.7259\mu\text{s}$ for all SWAP operations and $T = 2.3095\mu\text{s}$ for \sqrt{iSWAP} .

In addition to imperfections in rotation and phase adjustment, the short lifetime of Rydberg states is a significant source of decoherence in atomic processors. Adding spontaneous and BBR induced depopulation from the $100S_{1/2}$ Rydberg state of Cs with a lifetime of $400\mu\text{s}$ without a Cryogenic environment [66], the fidelity in Fig. 2 would be 99%, see table III. To compare this method with the conventional circuit model implemented with Rydberg gates, we define the time-integrated probability to be in the Rydberg state $\bar{T}_r = \int P_r(t)dt$ where $P_r(t)$ is the Rydberg population averaged over all qubit configurations at time t . For the parameter set of Fig. 2, the time-integrated Rydberg population over the gate operation is $\bar{T}_r = 2.4\mu\text{s}$. In an alternative circuit model, implementing the Fredkin gate requires eight C-NOT gates. Applying the Gaussian π pulse with the same laser intensity as in Fig. 2, for making the eight C-NOTs, the total time-integrated Rydberg population would be $\bar{T}_r = 21.7\mu\text{s}$. Hence, the proposed scheme suppresses the time integrated Rydberg population by an order of magnitude.

Moreover, we assess the resilience of our protocol to both laser-intensity noise and Doppler-induced dephasing. Thermal motion imparts a Doppler shift to each atom, producing a time-dependent detuning δ of the Rydberg-excitation lasers. We model these detunings as independent Gaussian random variables with $\langle \delta \rangle = 0$, $\sigma_\delta = k_{\text{eff}} v_{\text{rms}}$, where k_{eff} is the effective two-photon wavevector, and $v_{\text{rms}} = \sqrt{k_B T_a / M}$ is the root-mean-square atomic speed at temperature T_a and mass M . In our implementation with Cs, we use counter-propagating

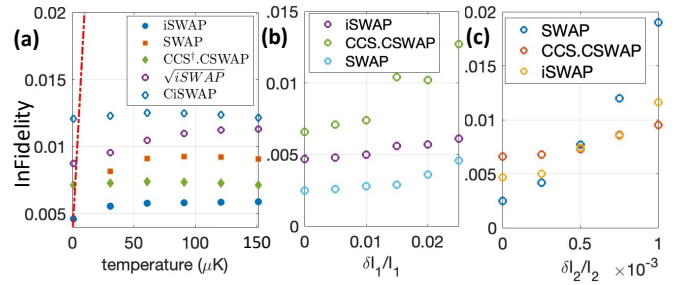


FIG. 3. Stability of the gate scheme against parameter fluctuations in (a) detuning, (b) Ω_1 , and (c) Ω_2 . (a) The infidelity caused by Doppler broadening due to atomic thermal motion is plotted as a function of temperature. The scattered signs denote the present scheme; the dotted-dashed curve shows the anti-blockade Fredkin-gate model from Ref. [61]. (b,c) Infidelity versus the relative Gaussian width of laser-intensity fluctuations for (b) Ω_1 and (c) Ω_2 . Each data point represents an average over 40 independent trials. The applied parameters are listed in Table I.

1040nm and 459.6nm fields to drive a two-photon transition from $|1\rangle$ to $|r\rangle$ via $|7P_{1/2}\rangle$. As shown in Fig. 3a, this configuration tolerates a vapor-cell temperature of $T_a \approx 150\mu\text{K}$, well above the $5\mu\text{k}$ required by the anti-blockade Rydberg Fredkin gate of [61], making experimental realization substantially more straightforward.

Laser-intensity fluctuations, stemming from beam-profile inhomogeneities or power-drift noise, translate into uncertainty in the Rabi frequencies $\Omega_{1,2}$. To suppress spatial inhomogeneity, one can employ a super-Gaussian (“flat-top”) beam profile [67]. Figures 3b and 3c simulate power-drift noise by adding, at each time step, independent Gaussian fluctuations to Ω_1 and Ω_2 characterized by their relative Gaussian width $\delta I/I$. The scheme exhibits greater tolerance to Ω_1 noise, while practical stabilization of Ω_2 suffices to maintain fidelity above the 99% level. For instance, modern 1040nm Ti:Sapphire lasers routinely achieve $\delta I_1/I_1 < 7.5 \times 10^{-4}$ over 10Hz-10MHz bandwidths [68], and 459nm sources can reach $\delta I_2/I_2 \lesssim 10^{-4}$ [69, 70].

To implement controlled operations between widely separated qubits in the lattice, we optimize the controlling parameters at different interatomic distances. Figure 4 illustrates how these parameters affect the rotation fidelity (excluding phase errors). Figure 4a shows that a modest ratio of Rabi frequencies ($\Omega_2 = 1.25 \Omega_1$) suffices, with the gate duration, and hence Rydberg decay, setting a lower bound on Ω_1 . By plotting the rotation infidelity against V/Ω_2 in Fig. 4c, two failure regimes become apparent. One in the weak interaction limit ($|V| \ll \Omega_2$) where the control atom cannot suppress the swap operation, see Fig. 2(a1). The second failure is caused by the interaction-induced resonance ($|V - \Delta| \ll \Omega_2$), see Fig. 2(a1,a6). The C-SWAP gate maintains high fidelity even for fairly weak interactions, down to $V = -1.5 \Omega_2$, see Fig. 4c. Finally, to evaluate the gate’s operational range, Fig. 4(d) shows the total infi-

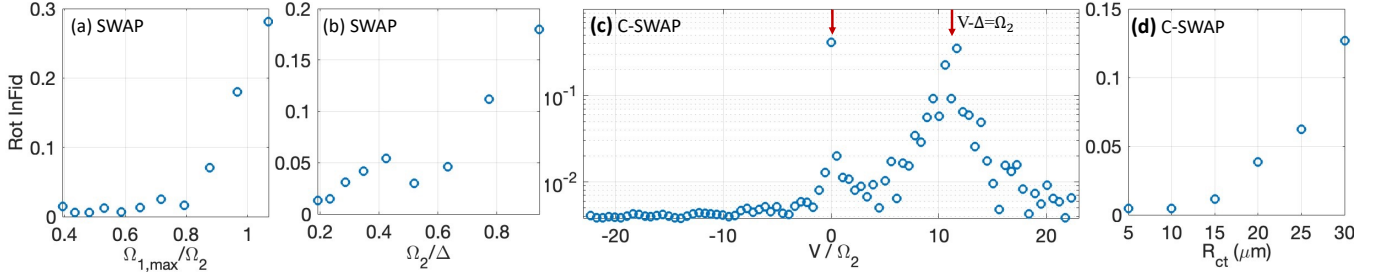


FIG. 4. **Optimum Parameters for LongRange Operation** – (a-c) Effects of the relative controlling parameters, on the rotation fidelity (excluding the phase adjustment). (d) The infidelity of C-SWAP versus interatomic distance, encountering the population rotation errors, and Rydberg loss. The applied parameters are the same as in Table I, except that in (a) Ω_{1max} , in (b) Ω_2 , in (c) V , and in (d), all parameters are optimized for each interatomic distance.

delity—including both rotation errors and Rydberg-state decay—as a function of the interatomic distance for a C-SWAP operation with atomic arrangement on a triangular geometry. To realize an attractive interaction, we employ the $|100P_{3/2}, 3/2\rangle$ Rydberg state with an interaction coefficient of $C_6 = -80 \text{ THz, } \mu\text{m}^6$, while all other control parameters are optimized accordingly. An alternative configuration uses $|70S_{1/2}, 1/2\rangle$ and $|67D_{5/2}, 5/2\rangle$ states for the control and target qubits, respectively, yielding a comparable attractive interaction strength and allowing excitation via a two-photon transition.

IV. EXTENSIONS TO MULTI-CONTROL AND MULTIPLEXED GATES

The scheme can be extended beyond the single-control Fredkin gate to realize a multi-control SWAP (C_k -SWAP), where k control qubits jointly regulate the exchange of two target registers. Considering the geometry of Fig. 5c, any two atoms lie within the mutual blockade range. Control qubits are sequentially excited from the $|0\rangle$ logic state to the Rydberg state before applying the target pulses of Fig. 1 and are de-excited in reverse order. In this configuration, the exchange channel becomes resonant only when all control qubits remain in the $|1\rangle$ qubit state, while any Rydberg excitation among them induces strong control-target interactions that block the SWAP. As shown in Fig. 4(c), for attractive control-target couplings, interaction strengths exceeding about $3\Omega_2$ are sufficient to block the exchange, ensuring that only the fully unexcited control configuration participates in the resonant transfer. This provides a compact and hardware-efficient realization of multi-flag conditional logic, directly applicable to syndrome-conditioned operations in quantum error correction, multi-copy state-verification protocols (e.g., multi-register SWAP tests), and heralded entanglement routing where several control nodes jointly authorize an exchange event.

A complementary generalization is the *conditional*

multiplexed SWAP, defined as

$$U = |0\rangle_c\langle 0| \otimes \text{SWAP}_{12} + |1\rangle_c\langle 1| \otimes \text{SWAP}_{34}, \quad (10)$$

where the control qubit determines which target pair undergoes exchange, see Fig. 5d. This operation realizes a conditional multi-path exchange, where the control qubit selects between two disjoint exchange channels. It functions as a quantum switchboard, coherently activating one of several communication links between independent register pairs. In superposition, the control can coherently engage multiple exchange pathways simultaneously, allowing interference-based routing and parallel quantum-state transfer. Such functionality provides a compact primitive for reconfigurable quantum networks and entanglement-routing protocols.

Using anisotropic Rydberg interactions, the control and target qubits can be arranged so that distinct target pairs couple through different Rydberg manifolds. The control qubit is excited via a π pulse from different logic qubits to either $|nP_{3/2}, 3/2\rangle$ or $|(n-1)D_{5/2}, 5/2\rangle$, while the four target atoms are driven by identical pulses of Fig. 1 in addressing the $|nS_{1/2}, 1/2\rangle$ Rydberg state. Exploiting the anisotropy of the nS-nP and nS-nD interactions, one target pair is aligned along the quantization axis, and the other is positioned at the magic angle $\theta = 54.7^\circ$, where their interaction contrast is maximized. This configuration renders the control-target couplings spin-dependent, enabling selective blockade of one target pair while leaving the other dark to the control interaction coupled, see Fig. 5d.

As discussed, in the four-photon SWAP process of Eq. 2, the exchange occurs only through the symmetric collective state $(|1r\rangle + |r1\rangle)/\sqrt{2}$. If either target qubit is blockaded by the Rydberg control, the intermediate single-excitation states $|1r\rangle$ or $|r1\rangle$ could not support the SWAP transition. In the four-target configuration, the control qubit thus blocks Rydberg excitation in one target pair while the other, free from control-induced interaction, would exclusively undergo the SWAP operation.

In a different three-target architecture of Fig. 5e, by arranging three target atoms such that target 1 always lies outside the control's blockade region, while targets

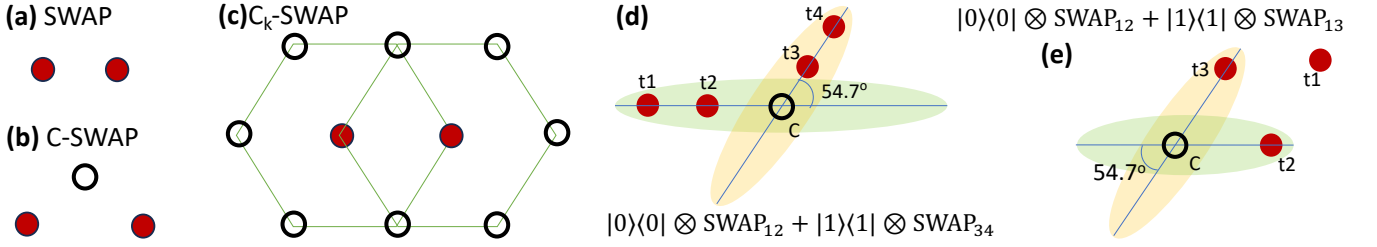


FIG. 5. **Geometry of extended SWAP and C-SWAP variants with higher-order generalizations.** Control and target qubits are represented by hollow and solid circles, respectively. Panels (a)–(c) illustrate the geometries of (a) a SWAP gate, (b) a controlled-SWAP (C-SWAP) gate, and (c) a multi-control SWAP (C_k -SWAP) gate, arranged in a triangular lattice configuration in which every pair of atoms resides within the mutual Rydberg blockade range. Panels (d,e) illustrate the geometries of conditional multiplexed SWAP gates. Different logical states of the control atom are coupled to distinct Rydberg levels, $|nP_{3/2}, 3/2\rangle$ or $|(n-1)D_{5/2}, 5/2\rangle$, while the targets are driven to $|nS_{1/2}, 1/2\rangle$. The resulting anisotropic control–target blockade regions, shown as green and yellow shaded areas, selectively inhibit the SWAP operation for blockaded targets. (d) Four-target configuration implementing Eq. 10. (e) Three-target architecture implementing Eq. 11, where target 1 always lies outside the control blockade, while targets 2 and 3 are blockaded conditionally on the control-qubit state.

2 and 3 are blockaded conditionally on the control qubit state, one can realize

$$U = |0\rangle_c \langle 0| \otimes \text{SWAP}_{12} + |1\rangle_c \langle 1| \otimes \text{SWAP}_{13}, \quad (11)$$

where the control qubit determines which secondary register (2 or 3) would exchange its quantum state with a shared site 1. Note that only the pair of target atoms that are not Rydberg-blocked by the control, but lie within each other’s blockade radius, can participate in the four-photon SWAP process via the symmetric collective state $(|1r\rangle + |r1\rangle)/\sqrt{2}$. Unlike the four-target design, which connects two independent pairs, this geometry introduces a common hub qubit that coherently couples to multiple destinations. Such a configuration acts as a coherent quantum memory port, enabling controlled transfer between two memory registers and a shared central node. In a networked setting, it provides quantum-controlled link selection, where the control qubit decides which remote site establishes a connection with the central hub. Because the process is fully coherent, superpositions of control states realize simultaneous and interference-based routing, establishing a hardware primitive for quantum random-access memory [71] and dynamically reconfigurable entanglement networks.

V. DISCUSSION AND OUTLOOK

In this work, we introduced and demonstrated a general interference-enabled mechanism for realizing native

exchange and controlled-exchange gates in neutral-atom quantum processors. By tuning a controllable near-degeneracy in the collective manifold of excited states, the scheme coherently toggles mediated exchange channels to perform single-step SWAP and controlled-SWAP (Fredkin) operations with fidelities exceeding 99% and an order-of-magnitude reduction in circuit depth and Rydberg exposure compared with decomposed implementations. The protocol remains robust against Doppler broadening at approximately 150 μK and realistic laser-intensity fluctuations, eliminating the need for evaporative cooling and reducing thermal and calibration demands in large-scale arrays.

Beyond single-control gates, the same interference principle enables (C_k -SWAP), where several control qubits jointly regulate SWAP operation. We also discussed conditional multiplexed SWAP extensions, where a control qubit regulates or selects among multiple exchange channels. These multi-path and multi-flag generalizations provide compact hardware primitives for conditional routing, multi-copy verification, and syndrome-conditioned logic, advancing the capability of neutral-atom systems toward coherent quantum routers and QRAM elements.

By elevating exchange to a native primitive alongside conditional phase operations, this work establishes a versatile tool set for neutral-atom computation. Our work may inspire the pursuit of similar programmable multi-qubit exchange in other architectures and mark a critical step toward scalable verification, efficient fermionic simulation, and hardware-level compilation across the broader landscape of quantum technologies.

[1] M. Saffman, T. G. Walker, and K. Mølmer, Quantum information with Rydberg atoms, *Rev. Mod. Phys.* **82**, 2313–2363 (2010).
[2] H. Busche, P. Huillery, S. W. Ball, T. Ilieva,

M. P. A. Jones, and C. S. Adams, “Contactless nonlinear optics mediated by long-range Rydberg interactions,” *Nat. Phys.* **13**, 655 (2017).
[3] M. Khazali, Ultratight confinement of atoms in a

Rydberg-empowered optical lattice, *Quantum* **9**, 1585 (2025).

[4] Ding, D. S., Busche, H., Shi, B. S., Guo, G. C., & Adams, C. S. Phase diagram and self-organizing dynamics in a thermal ensemble of strongly interacting Rydberg atoms. *Phys. Rev. X*, **10**, 021023 (2020).

[5] Stiesdal, N., Busche, H., Kleinbeck, K., Kumlin, J., G. Hansen, M., Büchler, H. P., & Hofferberth, S. Controlled multi-photon subtraction with cascaded Rydberg superatoms as single-photon absorbers. *Nature Communications*, **12**, 4328 (2021).

[6] L. Bombieri, Z. Zeng, R. Tricarico, R. Lin, S. Notarnicola, M. Cain, M. D. Lukin, and H. Pichler, “Quantum adiabatic optimization with Rydberg arrays: Localization phenomena and encoding strategies,” *PRX Quantum* **6**, 020306 (2025).

[7] N. Maskara, A. A. Michailidis, W. W. Ho, D. Bluvstein, S. Choi, M. D. Lukin, and M. Serbyn, “Discrete time-crystalline order enabled by quantum many-body scars: Entanglement steering via periodic driving,” *Phys. Rev. Lett.* **127**, 090602 (2021).

[8] M. Khazali, K. Heshami, C. Simon “Single-photon source based on Rydberg exciton blockade”, *J. Phys. B* **50**, 215301 (2017).

[9] H. Weimer *et al.*, A Rydberg quantum simulator, *Nat. Phys.* **6**, 382–388 (2010).

[10] M. Khazali, “Quantum information and computation with Rydberg atoms”, *IJAP* **10**, 19 (2021).

[11] D. Maxwell, D. J. Szwarc, D. P. Barato, H. Busche, J. D. Pritchard, A. Gauguet, K. J. Weatherill, M. P. A. Jones, and C. S. Adams, “Storage and control of optical photons using Rydberg polaritons,” *Phys. Rev. Lett.* **110**, 103001 (2013).

[12] H. Busche, S. Ball, P. Huillery, “A high repetition rate experimental setup for quantum non-linear optics with cold Rydberg atoms *Eur. Phys. J. Spec. Top.* **225**, 1131 (2016).

[13] M. Khazali, C. Murray, and T. Pohl, Polariton exchange interactions in multichannel optical networks, *Phys. Rev. Lett.* **123**, 113605 (2019).

[14] G. Semeghini, H. Levine, A. Keesling, S. Ebadi, ..., M. Greiner, V. Vuletić, and M. D. Lukin, “Probing topological spin liquids on a programmable quantum simulator,” *Science* **374**, 1242 (2021).

[15] S. Ebadi, et. al. “Quantum optimization of maximum independent set using Rydberg atom arrays,” *Science* **376**, 1209 (2022).

[16] M. Khazali, Rydberg noisy-dressing and applications in making soliton molecules and droplet quasi-crystals, *Phys. Rev. Res.* **3**, L032033 (2021).

[17] Z. Shi, M. Khazali, L. Qin, Y. Zhou, and Y. Zhong, Pattern formations and their active manipulation in a Rydberg noisy-dressed Bose–Einstein condensate, *Opt. Lett.* **49**, 6517–6520 (2024).

[18] S. Ebadi, T. T. Wang, H. Levine, A. Keesling, ..., M. Greiner, V. Vuletić, and M. D. Lukin, “Quantum phases of matter on a 256-atom programmable quantum simulator,” *Nature* **595**, 227 (2021).

[19] M. Khazali, Fast multicomponent cat-state generation under resonant or strong-dressing Rydberg-Kerr interaction, *Phys. Rev. A* **109**, 053716 (2024).

[20] D. Bluvstein, A. Omran, H. Levine, ..., M. Greiner, V. Vuletić, and M. D. Lukin, “Controlling quantum many-body dynamics in driven Rydberg atom arrays,” *Science* **371**, 136 (2021).

[21] M. Khazali, Progress towards macroscopic spin and mechanical superposition via Rydberg interaction, *Phys. Rev. A* **98**, 043836 (2018).

[22] M. Khazali, H. W. Lau, A. Humeniuk, and C. Simon, Large energy superpositions via Rydberg dressing, *Phys. Rev. A* **94**, 023408 (2016).

[23] C. Chen, G. Bornet, M. Bintz, ..., A. Browaeys, “Continuous symmetry breaking in a two-dimensional Rydberg array,” *Nature* **616**, 691 (2023).

[24] M.-T. Nguyen, J.-G. Liu, J. Wurtz, M. D. Lukin, S.-T. Wang, and H. Pichler, “Quantum optimization with arbitrary connectivity using Rydberg atom arrays,” *PRX Quantum* **4**, 010316 (2023).

[25] M. Khazali, Universal terminal for cloud quantum computing, *Sci. Rep.* **14**, 15412 (2024).

[26] D. Jaksch, J. I. Cirac, P. Zoller, S. L. Rolston, R. Côté, and M. D. Lukin, “Fast quantum gates for neutral atoms,” *Phys. Rev. Lett.* **85**, 2208 (2000).

[27] M. Khazali and K. Mølmer, Fast multi-qubit gates via adiabatic evolution in dark state manifolds of Rydberg atoms and superconducting circuits, *Phys. Rev. X* **10**, 021054 (2020).

[28] Levine, H., Keesling, A., Semeghini, G., Omran, A., Wang, T. T., Ebadi, S., ... & Lukin, M. D. Parallel implementation of high-fidelity multiqubit gates with neutral atoms. *Phys. Rev. Lett.* **123**, 170503 (2019).

[29] D. Møller, L. B. Madsen, and K. Mølmer, “Quantum gates and multiparticle entanglement by Rydberg excitation blockade and adiabatic passage,” *Phys. Rev. Lett.* **100**, 170504 (2008).

[30] M. Khazali and W. Lechner, Scalable quantum processors empowered by the Fermi scattering of Rydberg electrons, *Commun. Phys.* **6**, 57 (2023).

[31] D. Bluvstein *et al.*, Logical quantum processor based on reconfigurable atom arrays, *Nature* **626**, 58–65 (2024).

[32] M. Khazali, All-optical quantum information processing via a single-step Rydberg blockade gate, *Opt. Express* **31**, 13970–13980 (2023).

[33] M. Khazali, K. Heshami, and C. Simon, Photon-photon gate via the interaction between two collective Rydberg excitations, *Phys. Rev. A* **91**, 030301(R) (2015).

[34] L. S. Theis, F. Motzoi, F. K. Wilhelm, and M. Saffman, “High-fidelity Rydberg-blockade entangling gate using shaped, analytic pulses,” *Phys. Rev. A* **94**, 032306 (2016).

[35] A. Gaëtan, Y. Miroshnychenko, T. Wilk, A. Chotia, M. Viteau, D. Comparat, P. Pillet, A. Browaeys, and P. Grangier, “Observation of collective excitation of two individual atoms in the Rydberg blockade regime,” *Nat. Phys.* **5**, 115 (2009).

[36] E. Urban, T. A. Johnson, T. Henage, L. Isenhower, D. D. Yavuz, T. G. Walker, and M. Saffman, “Observation of Rydberg blockade between two atoms,” *Nat. Phys.* **5**, 110 (2009).

[37] T. Wilk, A. Gaëtan, C. Evellin, J. Wolters, Y. Miroshnychenko, P. Grangier, and A. Browaeys, “Entanglement of two individual neutral atoms using Rydberg blockade,” *Phys. Rev. Lett.* **104**, 010502 (2010).

[38] L. Isenhower, E. Urban, X. L. Zhang, A. T. Gill, T. Henage, T. A. Johnson, T. G. Walker, and M. Saffman, “Demonstration of a neutral atom controlled-NOT quantum gate,” *Phys. Rev. Lett.* **104**, 010503 (2010).

[39] A. W. Carr and M. Saffman, “Preparation of entan-

gled and antiferromagnetic states by dissipative Rydberg pumping," *Phys. Rev. Lett.* **111**, 033607 (2013).

[40] D. Barredo, H. Labuhn, S. Ravets, T. Lahaye, A. Browaeys, and C. S. Adams, "Demonstration of a strong Rydberg blockade in three-atom systems with anisotropic interactions," *Phys. Rev. Lett.* **112**, 183002 (2014).

[41] A. Momtaheni, M. Khazali, "Quantum computation with longlived Rydberg-Landau atoms featuring suppressed ionization by the Magnetic Cage", arXiv:2506.00575 (2025)

[42] T. M. Graham, M. Kwon, B. Grinkemeyer, Z. Marra, X. Jiang, M. T. Lichtman, Y. Sun, M. Ebert, and M. Saffman, "Rydberg-mediated entanglement in a two-dimensional neutral atom qubit array," *Phys. Rev. Lett.* **123**, 230501 (2019).

[43] M. Khazali," Quasi-Contact Forces with Resonant Range Control in Rydberg Atoms", arXiv:2507.17361 (2025)

[44] S. Evered, et al. High-fidelity parallel entangling gates on a neutral-atom quantum computer. *Nature* **622**, 7982 (2023).

[45] H. Buhrman, R. Cleve, J. Watrous, and R. de Wolf, "Quantum fingerprinting," *Phys. Rev. A* **60**, 2737 (1999).

[46] A. K. Ekert, C. M. Alves, D. K. L. Oi, M. Horodecki, P. Horodecki, and L. C. Kwek, "Direct estimation of linear and nonlinear functionals of a density matrix," *Phys. Rev. Lett.* **88**, 217901 (2002).

[47] Buhrman, H., Cleve, R., Watrous, J. & Wolf, R. D. Quantum fingerprinting. *Phys. Rev. Lett.* **87**, 167902 (2001).

[48] R. Islam, R. Ma, P. M. Preiss, M. E. Tai, A. Lukin, M. Rispoli, and M. Greiner, "Measuring entanglement entropy in a quantum many-body system," *Nature* **528**, 77 (2015).

[49] L. Cincio, Y. Subaşı, A. T. Sornborger, and P. J. Coles, "Learning the overlap between quantum states," *npj Quantum Inf.* **7**, 87 (2021).

[50] A. Barenco, C. H. Bennett, R. Cleve, D. P. DiVincenzo, N. Margolus, P. Shor, T. Sleator, J. A. Smolin, and H. Weinfurter, "Elementary gates for quantum computation," *Phys. Rev. A* **52**, 3457 (1995).

[51] P. Roushan *et al.*, "Spectroscopic signatures of localization with interacting photons in superconducting qubits," *Nature Phys.* **13**, 146 (2017).

[52] C. Song *et al.*, "Generation of multicomponent atomic Schrödinger cat states of up to 20 qubits," *Science* **364**, 878 (2019).

[53] I. Bloch, J. Dalibard, and S. Nascimbène, "Quantum simulations with ultracold quantum gases," *Nature Phys.* **8**, 267 (2012).

[54] N. M. Linke, D. Maslov, M. Roetteler, S. Debnath, C. Figgatt, K. A. Landsman, K. Wright, and C. Monroe, "Experimental comparison of two quantum computing architectures," *Proc. Natl. Acad. Sci. USA* **114**, 3305 (2017).

[55] Ozaydin, F., Bugu, S., Yesilyurt, C., Altintas, A. A., Tame, M. & Özdemir, S. K. Fusing multiple W states simultaneously with a Fredkin gate. *Phys. Rev. A* **89**, 042311 (2014).

[56] Hofmann, H. F. How weak values emerge in joint measurements on cloned quantum systems. *Phys. Rev. Lett.* **109**, 020408 (2012).

[57] V. V. Shende, S. S. Bullock, and I. L. Markov, "Recognizing small-circuit structure in two-qubit operators," *Phys. Rev. A* **70**, 012310 (2004).

[58] A. M. Childs, E. Farhi, and S. Gutmann, "An example of the difference between quantum and classical random walks," *Phys. Rev. A* **68**, 052311 (2003).

[59] M. Khazali, "Discrete-Time Quantum-Walk & Floquet Topological Insulators via Distance-Selective Rydberg-Interaction", *Quantum* **6**, 664 (2022).

[60] D. Bluvstein, H. Levine, G. Semeghini, T. T. Wang, S. Ebadi, M. Kalinowski, A. Keesling, and M. Greiner, "A quantum processor based on coherent transport of entangled atom arrays," *Nature* **604**, 451 (2022).

[61] Wu, J. L., Wang, Y., Han, J. X., Su, S. L., Xia, Y., Jiang, Y. & Song, J. Unselective ground-state blockade of Rydberg atoms for implementing quantum gates. *Front. Phys.* **17**, 22501 (2022).

[62] Although the microwave field is globally applied, only the selected target atoms are tuned to the desired transition using a focused optical laser that locally shifts their qubit transition frequencies [63]. The remaining atoms in the array stay far detuned. For the idle atoms, the residual far-off-resonant coupling produces only a small, static AC Stark shift that is identical across the array. This global phase shift can be absorbed into the computational reference frame.

[63] Weitenberg, C., Endres, M., Sherson, J. F., Cheneau, M., Schauß, P., Fukuhara, T., Bloch, I. & Kuhr, S. Single-spin addressing in an atomic Mott insulator. *Nature* **471**, 319-324 (2011).

[64] Kim, T. & Choi, B. S. Efficient decomposition methods for controlled-Rn using a single ancillary qubit. *Sci. Rep.* **8**, 5445 (2018).

[65] L. H. Pedersen, N. M. Møller, and K. Mølmer, Fidelity of Quantum Operations, *Phys. Lett. A* **367**, 47 (2007).

[66] Beterov, I. I., et al. Quasiclassical calculations of blackbody-radiation-induced depopulation rates and effective lifetimes of Rydberg n S, n P, and n D alkali-metal atoms with $n < 80$ *Phys. Rev. A* **79**, 052504 (2009).

[67] Gillen-Christandl, K. *et al.* Comparison of Gaussian and super Gaussian laser beams for addressing atomic qubits. *Appl. Phys. B* **122**, 1–20 (2016).

[68] Solidstate Ti:Sa Laser System. <https://m2lasers.com/solstis.html>.

[69] Legaie, R., Picken, C. J., & Pritchard, J. D. Sub-kilohertz excitation lasers for quantum information processing with Rydberg atoms. *J. Opt. Soc. Am. B* , **35**, 892 (2018).

[70] Shi, T., Pan, D., & Chen, J. An inhibited laser. *Comms. Phys.* **5**, 208 (2022).

[71] G. Giovannetti, S. Lloyd, and L. Maccone, "Quantum Random Access Memory," *Phys. Rev. Lett.* **100**,160501(2008).

	SWAP	iSWAP	\sqrt{iSWAP}
Rot	$\begin{pmatrix} 1 & 0 & 0 & 0 \\ 0 & 0 & 0.9962 & 0 \\ 0 & 0.9962 & 0 & 0 \\ 0 & 0 & 0 & 0.974e^{-i\frac{7\pi}{1000}} \end{pmatrix}$	$\begin{pmatrix} 1 & 0 & 0 & 0 \\ 0 & 0 & 0.9933e^{i\frac{513\pi}{1000}} & 0 \\ 0 & 0.9933e^{i\frac{513\pi}{1000}} & 0 & 0 \\ 0 & 0 & 0 & 0.9973e^{-i\frac{9\pi}{1000}} \end{pmatrix}$	$\begin{pmatrix} e^{-i\frac{\pi}{1000}} & 0 & 0 & 0 \\ 0 & 0.7028e^{-i\frac{11\pi}{1000}} & 0.7045e^{i\frac{4949\pi}{1000}} & 0 \\ 0 & 0.7045e^{i\frac{4949\pi}{1000}} & 0.7028e^{-i\frac{11\pi}{1000}} & 0 \\ 0 & 0 & 0 & 0.999e^{-i\frac{4\pi}{100}} \end{pmatrix}$
Ryd-Loss	$\begin{pmatrix} 0.0003 & 0 & 0 & 0 \\ 0 & 0 & 0.0002 & 0 \\ 0 & 0.0002 & 0 & 0 \\ 0 & 0 & 0 & 0.0002 \end{pmatrix}$	$\begin{pmatrix} 0.0002 & 0 & 0 & 0 \\ 0 & 0 & 0.0002 & 0 \\ 0 & 0.0002 & 0 & 0 \\ 0 & 0 & 0 & 0.0003 \end{pmatrix}$	$\begin{pmatrix} 0.0002 & 0 & 0 & 0 \\ 0 & 0.00003 & 0.00003 & 0 \\ 0 & 0.00003 & 0.00003 & 0 \\ 0 & 0 & 0 & 0.00014 \end{pmatrix}$

TABLE II. **Numerically simulated state amplitudes and Rydberg loss for SWAP-type gates.** The upper matrices present the numerically obtained output state amplitudes, evolved from the corresponding input qubit product states under the parameters listed in Table I. The lower matrices show the population loss from the Rydberg state during the operation. Reported phase factors correspond to the final gate output after the single-qubit phase adjustments indicated in Table I.

	C-iSWAP							(C-SWAP) (CCS †)								
Rotation	$\begin{pmatrix} 1.0000 & 0 & 0 & 0 & 0 & 0 & 0 & 0 \\ 0 & 1.0000 & 0 & 0 & 0 & 0 & 0 & 0 \\ 0 & 0 & 1.0000 & 0 & 0 & 0 & 0 & 0 \\ 0 & 0 & 0 & 0.9985 & 0 & 0 & 0 & 0 \\ 0 & 0 & 0 & 0 & 1.0000 & 0 & 0 & 0 \\ 0 & 0 & 0 & 0 & 0 & 0 & 0.9910 & 0 \\ 0 & 0 & 0 & 0 & 0 & 0 & 0.9910 & 0 \\ 0 & 0 & 0 & 0 & 0 & 0 & 0 & 1.0000 \end{pmatrix}$							$\begin{pmatrix} 1 & 0 & 0 & 0 & 0 & 0 & 0 & 0 \\ 0 & 0.9995 & 0 & 0 & 0 & 0 & 0 & 0 \\ 0 & 0 & 0.9995 & 0 & 0 & 0 & 0 & 0 \\ 0 & 0 & 0 & 0.9998 & 0 & 0 & 0 & 0 \\ 0 & 0 & 0 & 0 & 0.9999 & 0 & 0 & 0 \\ 0 & 0 & 0 & 0 & 0 & 0 & 0.9988 & 0 \\ 0 & 0 & 0 & 0 & 0 & 0.9988 & 0 & 0 \\ 0 & 0 & 0 & 0 & 0 & 0 & 0 & 0.9998 \end{pmatrix}$								
Phase	$\begin{pmatrix} e^{-i\frac{8\pi}{100}} & 0 & 0 & 0 & 0 & 0 & 0 & 0 \\ 0 & e^{-i\frac{39\pi}{1000}} & 0 & 0 & 0 & 0 & 0 & 0 \\ 0 & 0 & e^{-i\frac{39\pi}{1000}} & 0 & 0 & 0 & 0 & 0 \\ 0 & 0 & 0 & e^{-i\frac{162\pi}{10000}} & 0 & 0 & 0 & 0 \\ 0 & 0 & 0 & 0 & e^{-i\frac{7\pi}{10000}} & 0 & 0 & 0 \\ 0 & 0 & 0 & 0 & 0 & e^{-i\frac{52\pi}{100}} & 0 & 0 \\ 0 & 0 & 0 & 0 & 0 & e^{-i\frac{52\pi}{100}} & 0 & 0 \\ 0 & 0 & 0 & 0 & 0 & 0 & e^{-i\frac{37\pi}{1000}} & 0 \end{pmatrix}$							$\begin{pmatrix} e^{-i\frac{76\pi}{1000}} & 0 & 0 & 0 & 0 & 0 & 0 & 0 \\ 0 & e^{-i\frac{44\pi}{1000}} & 0 & 0 & 0 & 0 & 0 & 0 \\ 0 & 0 & e^{-i\frac{44\pi}{1000}} & 0 & 0 & 0 & 0 & 0 \\ 0 & 0 & 0 & e^{-i\frac{4\pi}{100}} & 0 & 0 & 0 & 0 \\ 0 & 0 & 0 & 0 & e^{-i\frac{4\pi}{1000}} & 0 & 0 & 0 \\ 0 & 0 & 0 & 0 & 0 & e^{-i\frac{\pi}{100}} & 0 & 0 \\ 0 & 0 & 0 & 0 & 0 & 0 & e^{-i\frac{\pi}{100}} & 0 \\ 0 & 0 & 0 & 0 & 0 & 0 & 0 & e^{1.44i\pi} \end{pmatrix}$								
Rydberg Loss	$\begin{pmatrix} 0.011 & 0 & 0 & 0 & 0 & 0 & 0 & 0 \\ 0 & 0.011 & 0 & 0 & 0 & 0 & 0 & 0 \\ 0 & 0 & 0.011 & 0 & 0 & 0 & 0 & 0 \\ 0 & 0 & 0 & 0.011 & 0 & 0 & 0 & 0 \\ 0 & 0 & 0 & 0 & 0.0003 & 0 & 0 & 0 \\ 0 & 0 & 0 & 0 & 0 & 0.0002 & 0 & 0 \\ 0 & 0 & 0 & 0 & 0 & 0.0002 & 0 & 0 \\ 0 & 0 & 0 & 0 & 0 & 0 & 0.0002 & 0 \end{pmatrix}$								$\begin{pmatrix} 0.011 & 0 & 0 & 0 & 0 & 0 & 0 & 0 \\ 0 & 0.011 & 0 & 0 & 0 & 0 & 0 & 0 \\ 0 & 0 & 0.011 & 0 & 0 & 0 & 0 & 0 \\ 0 & 0 & 0 & 0.011 & 0 & 0 & 0 & 0 \\ 0 & 0 & 0 & 0 & 0.0007 & 0 & 0 & 0 \\ 0 & 0 & 0 & 0 & 0 & 0 & 0.0002 & 0 \\ 0 & 0 & 0 & 0 & 0 & 0.0002 & 0 & 0 \\ 0 & 0 & 0 & 0 & 0 & 0 & 0 & 0.00008 \end{pmatrix}$							

TABLE III. **Numerically simulated amplitudes, phase evolution, and Rydberg loss for controlled-SWAP-type gates.** The matrices in each block present the numerically simulated state amplitudes obtained by evolving the corresponding input qubit product states under the parameters of Table I. The three rows respectively show (i) the rotation amplitudes representing population transfer between computational basis states, (ii) the accumulated phase of each output component, and (iii) the population loss from the Rydberg state during the gate operation. Reported values correspond to the final gate output after applying the single-qubit phase adjustments specified in Table I.